Inorganic Chemistry

pubs.acs.org/IC

Article

Boosting Interfacial Charge Transfer with a Giant Internal Electric Field in a TiO_2 Hollow-Sphere-Based S-Scheme Heterojunction for Efficient CO_2 Photoreduction

Haiwei Su, Weikang Wang,* Haopeng Jiang, Lijuan Sun, Tingting Kong,* Zhongxi Lu, Hua Tang, Lele Wang, and Qinqin Liu*

Cite This: https://doi.org/10.1021/acs.inorgchem.2c02443

Read Online

ACCESS | Metrics & More | Article Recommendations | Supporting Information

ABSTRACT: The construction of an S-scheme charge transfer pathway is considered to be a powerful way to inhibit charge recombination and maintain photogenerated carriers with high redox capacity to meet the kinetic requirements of the carbon dioxide (CO_2) photoreduction reaction. For an S-scheme heterojunction, an internal electric field (IEF) is regarded as the main driving force for accelerating the interfacial spatial transfer of photogenerated charges. Herein, we designed a TiO_2 hollow-sphere (TH)-based S-scheme heterojunction for efficient CO_2 photoreduction, in which WO_3 nanoparticles (WP) were applied as an oxidation semiconductor to form an intimate interfacial contact with the TH. The S-scheme charge transfer mode driven by a strong IEF for the TH/WP composite was confirmed by *in situ* X-ray photoelectron spectroscopy and ultraviolet photoelectron spectroscopy. As a result, abundant photogenerated electrons with strong reducing ability would take part in the CO_2 reduction reaction. The combination of surface photovoltage spectra and transient photocurrent experiments disclosed that the IEF intensity and charge separation efficiency of the fabricated TH/WP composite were nearly 16.80- and 1.42-fold higher, respectively, than those of the pure TH. Furthermore, sufficient active sites provided by the hollow-sphere structure also enhanced the kinetics of the catalytic reaction. Consequently, the optimized TH/WP composite showed a peak level of CO production of 14.20 μmol g^{-1} in 3 h without the addition of any sacrificial agent. This work provides insights into the kinetic studies of the S-scheme charge transfer pathway for realizing high-performance CO_2 photoreduction.

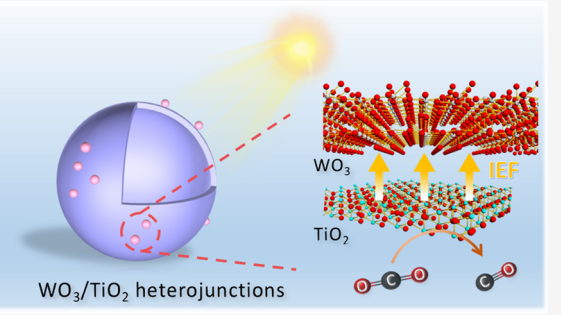

1. INTRODUCTION

The excessive consumption of traditional fossil fuels and the growing emission of greenhouse gas (CO_2) have led to emerging global energy and environmental crises.[1−3] Photocatalytic CO_2 reduction based on solar energy offers a sustainable strategy for converting CO_2 to generate fuels and chemicals to reduce the level of CO_2 in the atmosphere.[4] Nevertheless, efforts to decrease the level of CO_2 are still unsatisfying on a large scale due to the severe charge recombination and sluggish kinetics of photocatalysts. To promote the separation and transfer of photogenerated electrons and holes, numerous strategies have been developed for the design of efficient and cost-effective nanocatalysts, including heteroatom doping,[5] metal cocatalyst loading,[6] defect or crystal engineering,[7] nanostructure control,[8] and heterojunction construction.[9] Specifically, the step (S)-scheme heterojunction composed of reduction and oxidation photocatalysts has been proven to be a promising solution for the kinetic control of photogenerated charges.[10−12] In an S-scheme photocatalyst, an internal electric field (IEF) would occur at the interface were the two components with different Fermi energy levels to contact with each other in an S-scheme heterojunction. The IEF makes the main contribution to directional charge transfer and rapid recombination of invalid charges in the S-scheme transfer pathway,[13] leading to the improved spatial separation and transfer efficiency of photogenerated charges with the highest redox capacity being realized.[14,15] Thus, an effective IEF is crucial for constructing an S-scheme heterojunction that can satisfy the kinetic requirements of photogenerated charge transfer and CO_2 reduction.

Since the pioneering work of Fujishima and Honda,[16] nano titanium dioxide (TiO_2)-based catalytic systems have been studied extensively in solar energy conversion and environmental remediation.[17] As a representative photocatalyst, TiO_2 with its advantages of a suitable conduction band (CB) level,[18]

Received: July 12, 2022

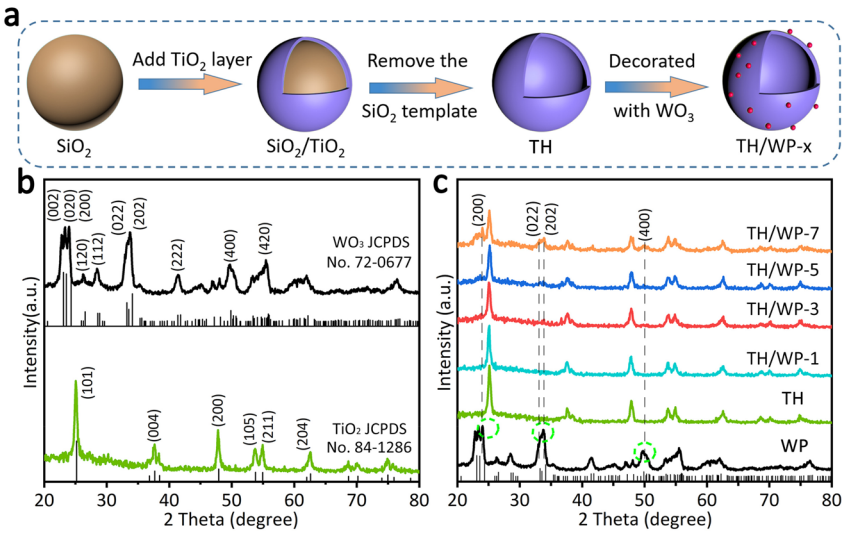

Figure 1. (a) Schematic diagram for the synthesis of TH/WP composite. XRD patterns of (b) the TH and WP samples and (c) the TH, WP, and TH/WP-*x* samples with different WP loading contents.

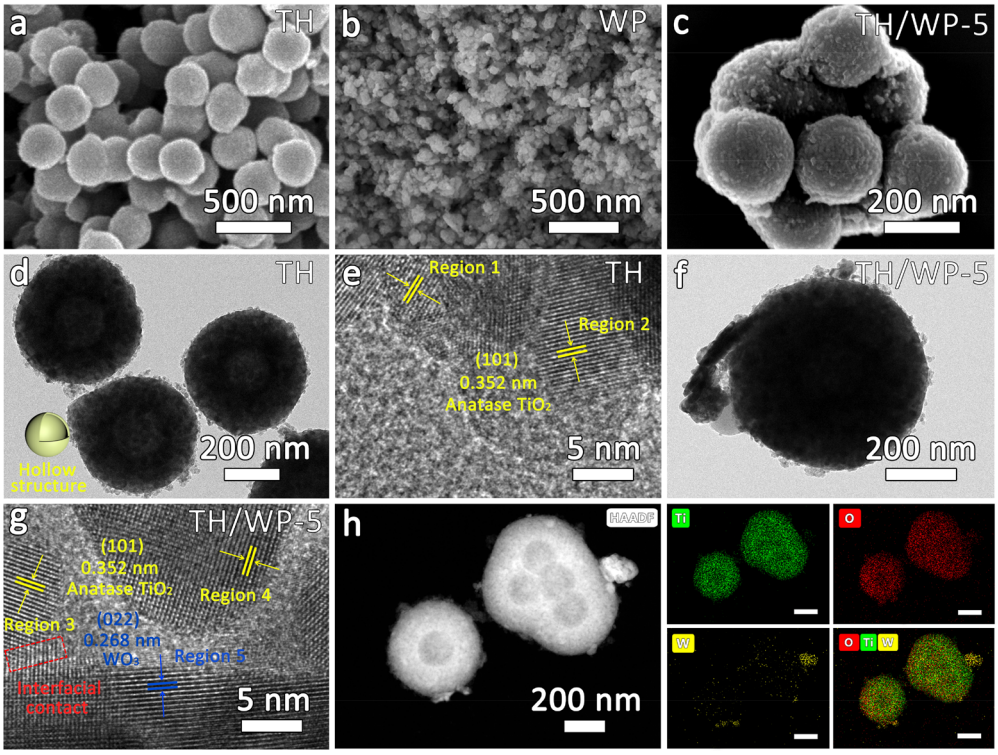

Figure 2. SEM images of the (a) TH, (b) WP, and (c) TH/WP composite. TEM and HRTEM images of the (d and e) pure TH and (f and g) TH/WP heterojunction. (h) HAADF-STEM image and elemental mapping of the TH/WP heterojunction.

high chemical stability,[19] low cost,[20] and nontoxicity[21] is considered as an ideal candidate for CO_2 photoreduction.[22] However, the disordered free diffusion and slow transfer efficiency of photogenerated charges in TiO_2 would lead to insufficient surface electrons and a low apparent quantum efficiency for CO_2 photoreduction. Morphological control of TiO_2 is shown to be an appropriate resolution for promoting photocatalytic performance, including hierarchical,[23] hollow-sphere,[24] yolk−shell,[25] and other novel structures. In particular, the hollow structure can enhance the light-harvesting efficiency due to the multiscattering of incident light.[26] In addition, more exposed active sites in the hollow structure would provide more efficient sites for CO_2 adsorption and conversion. In 2021, Wang et al. developed a TiO_2 hollow-sphere integrated with an N-doped graphene layer that demonstrated enhanced light absorption and a high CO_2 photoreduction performance of 18.11 μmol g^{-1} h^{-1}.[27] Meanwhile, the hollow-sphere structure can act as a superior platform for the construction of a heterojunction composite. To gain a deeper understanding of the IEF in S-scheme heterojunctions, we must find a suitable oxidation photocatalyst to combine with the TiO_2 hollow sphere to form a reliable S-scheme. Specifically, tungsten oxide (WO_3) is selected as an ideal oxidation photocatalyst with a large work

https://doi.org/10.1021/acs.inorgchem.2c02443
Inorg. Chem. XXXX, XXX, XXX−XXX

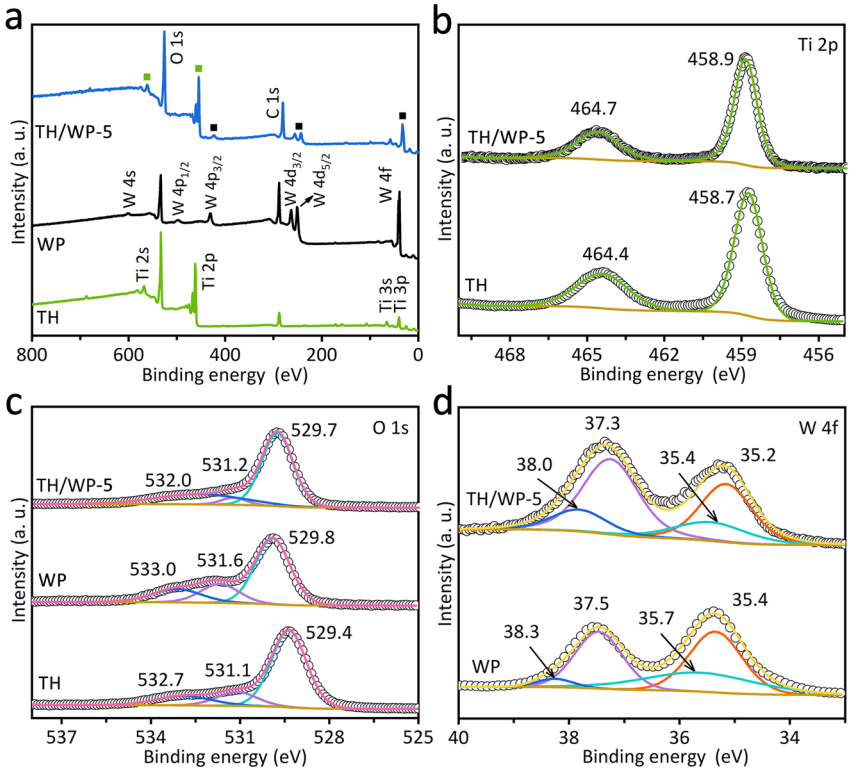

Figure 3. (a) XPS full spectra and (b) Ti 2p, (c) O 1s, and (d) W 4f high-resolution spectra of different samples.

function, superior photovoltaic properties, an easily scalable synthesis, and strong oxidation capacity for the constructiono of an efficient S-scheme photocatalyst with a TiO_2 hollow sphere.[28]

Herein, we construct an S-scheme heterojunction composed of a TiO_2 hollow sphere (TH) and WO_3 nanoparticles (WP) as a model in this work, in which the WP formed an intimate plane contact with the TH, contributing to the establishment of a giant IEF for directional carrier transfer and charge separation. The S-scheme charge transfer mechanism of the TH/WP composites can be confirmed by *in situ*-irradiated X-ray photoelectron spectroscopy (XPS) and work function tests,[29] and the intensity of the IEF established in the S-scheme can be tested by transient photocurrent response plots and steady-state surface photovoltage (SS-SPV) spectra.[30] The experimental results demonstrated that the strong IEF established in the S-scheme heterojunction improved the photogenerated charge transfer kinetics and CO_2 photoreduction performance. The as-prepared TH/WP composite exhibited a significantly enhanced CO_2 reduction performance, the rate of production of CO reaching 4.73 μmol g^{-1} h^{-1} without any sacrificial agents.

2. RESULTS AND DISCUSSION

Figure 1a illustrates the synthesis of the TH/WP heterojunction photocatalysts. The TH is first constructed via a modified silicon dioxide (SiO_2) template method. Meanwhile, the WP is synthesized by a facile hydrothermal method and annealing treatment, forming a nanoparticle structure with a radius of ~20 nm. Finally, the TH/WP-*x* S-scheme heterojunction composites are obtained by a liquid-phase mixing process. The X-ray diffraction (XRD) patterns of the WP, TH, and TH/WP-*x* samples were recorded to investigate their crystal structure. It is notable in Figure 1b that the strong peaks at 23.99°, 33.17°, 33.72°, and 49.75° that occurred in the XRD pattern of WP can be assigned to the (200), (202), and (400) planes of monoclinic WO_3 (JCPDS Card 72-0677).[31] Moreover, the peaks at 25.05°, 37.65°, 47.8°, 53.75°, 54.94°, and 62.57° are assigned to the (101), (004), (200), (105), (211), and (204) planes of TiO_2, respectively (JCPDS Card 84-1286),[29] indicating the anatase phase of the TH. The XRD patterns of a series of TH/WP-*x* composites with different amounts of the WP added are shown in Figure 1c. Nevertheless, the characteristic diffraction peaks of WP can barely be observed in XRD patterns of composites, due to the relatively low loading content. Only when the WP:TH mass ratio reached 7% did the main peaks corresponding to the (200), (022), (202), and (400) planes appear. Compared with those of the pristine WP and TH, the diffraction peak positions of TH/WP-*x* composites are almost unchanged, indicating that the crystal structures of WP and TH remain intact.

The morphology of the TH/WP photocatalysts was investigated by scanning electron microscope (SEM) and transmission electron microscope (TEM) images. As shown in Figure 2a, the TiO_2 etched with a HF solution exhibits a uniform hollow sphere with a diameter of ~400 nm. Meanwhile, the size distribution of the prepared WP is even, ~20 nm (Figure 2b). Obviously, Figure 2c shows for the TH/WP composites that the WP are scattered on the outer surface of the TH spherical shell with intimate contact, forming a dual-shell hollow-sphere structure. The TEM image of the TH is shown in Figure 2d, indicating a hollow structure of the pristine TH with a uniform spherical shell (thickness of ~100 nm). Accordingly, the high-resolution TEM (HRTEM) image in Figure 2e of the TH indicates an interplanar distance of 0.352 nm (Figure S1), which belongs to the (101) crystal plane of anatase TiO_2, further verifying the anatase phase of the TH.[32] In addition, the TEM image of the TH/WP

https://doi.org/10.1021/acs.inorgchem.2c02443
Inorg. Chem. XXXX, XXX, XXX−XXX

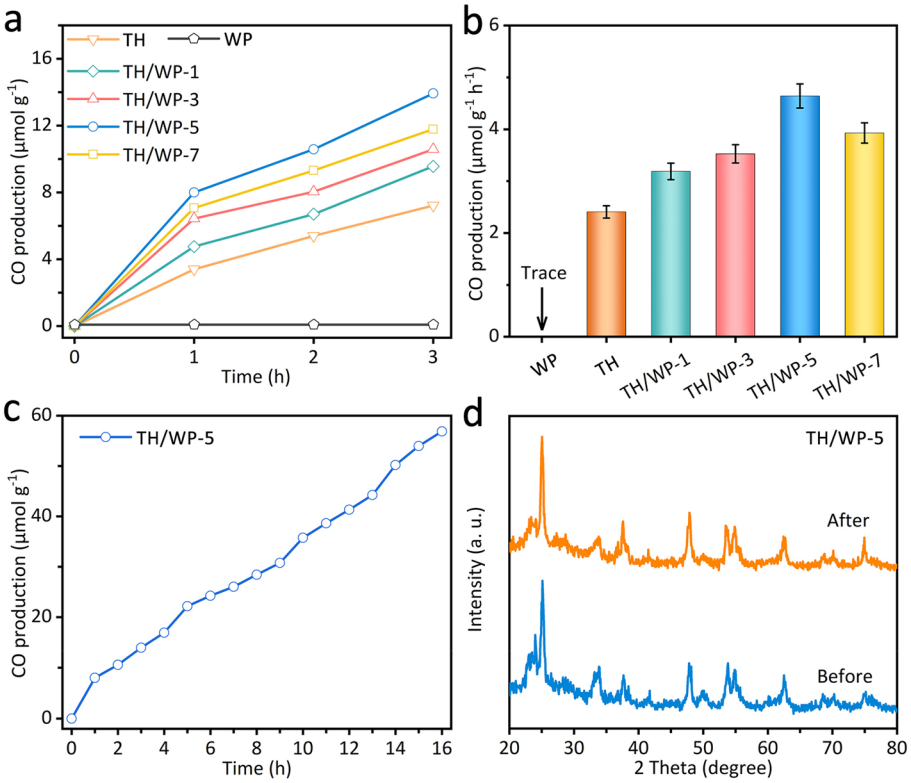

Figure 4. (a) Time course of CO production and (b) CO production rate over the pristine WP, TH, and TH/WP-*x* heterojunction with different WP contents. (c) CO production performance of the TH/WP-5 composite under continuous irradiation for 16 h. (d) XRD patterns before and after CO_2 photoreduction.

composites (Figure 2f) shows that the hollow-sphere morphology of the TH is well maintained, and the WP uniformly attached on the outer wall of the TH. As illustrated in the HRTEM image of the TH/WP composite (Figure 2g), the interplanar distances are 0.352 and 0.268 nm (Figure S2), corresponding to the anatase TiO_2 (101) and WO_3 (022) crystal planes, respectively.[31] The tight interfacial contact between the TH and WP could also be observed in the red square. Furthermore, the elemental distribution mapping of a high-angle annular dark field scanning transmission electron microscope (HAADF-STEM) image in Figure 2h shows that there are three elements (Ti, W, and O) in the TH/WP composite with a homogeneous distribution, which further proves the successful synthesis of the TH/WP composite.

Meanwhile, the anatase TiO_2 nanoparticles [TP (Figure S3)] were prepared for comparison with the TiO_2 hollow-sphere structure. The N_2 absorption−desorption isotherms of TH and TH/WP-5 were recorded and are presented in Figure S4a, which demonstrated a type IV isotherm with an H3-type hysteresis loop illustrating their porous characteristics. Moreover, the Brunauer−Emmett−Teller (BET) specific surface areas of TH and TH/WP-5 are 105.61 and 107.70 $m^2\ g^{-1}$, respectively, significantly larger than that of TP (17.62 $m^2\ g^{-1}$). The corresponding pore size distribution curves of prepared samples based on the desorption curves are shown in Figure S4b. The larger BET specific surface area of TH/WP-5 would provide more active sites for CO_2 adsorption and activation, favoring the photocatalytic reaction.[33]

The surface elemental compositions and chemical states of the TH, WP, and TH/WP composite were investigated by X-ray photoelectron spectroscopy (XPS). The XPS full spectra (Figure 3a) show that all O, Ti, and W elements are displayed in the TH/WP sample, while no other elements can be found, which is consistent with the mapping element distribution results (Figure 2h). The actual elemental contents of O, Ti, and W are listed in Table S1. The shift in the binding energy peaks in high-resolution XPS spectra can directly reflect the change in the electron density of elements.[34] In Figure 3b, the binding energy peaks in high-resolution Ti 2p XPS spectra of the TH center at 458.7 and 464.4 eV could be attributed to the $2p_{3/2}$ and $2p_{1/2}$ orbitals of Ti^{4+}, respectively.[35] Moreover, the O 1s spectra (Figure 3c) of the TH show that the peaks centered at binding energies of 529.4, 531.1, and 532.7 eV are attributed to metal lattice oxygen, a surface hydroxyl group (-OH), and adsorbed oxygen, respectively.[36] For the W element (Figure 3d) of the WP, the peaks at binding energies of 35.4 and 37.5 eV are attributed to the $4f_{7/2}$ and $4f_{5/2}$ orbitals of W^{6+}, respectively, while the two lower-binding energy peaks at 35.7 and 38.3 eV belong to W^{5+}.[37] The existence of W^{5+} is probably caused by the O vacancies in the WP.

Notably, the Ti 2p binding energies in the TH/WP heterojunction increase with a large offset of 0.3 eV compared with those of the TH, while its W 4f binding energy peaks shift to a lower binding energy (~0.2 eV) compared with those of the WP. The results indicate that electrons in the TH/WP could spontaneously transfer from TH to WP, when the TH and WP contact with each other, leading to the band bending and IEF formed on the interface between two components. This phenomenon can provide strong evidence of the formation of the TH/WP S-scheme heterojunction.

The photocatalytic CO_2 reduction tests of different samples were carried out under visible light irradiation in pure water without the addition of any sacrificial agents or cocatalysts (Figures S5 and S6). Obviously, the amount of CO product

https://doi.org/10.1021/acs.inorgchem.2c02443
Inorg. Chem. XXXX, XXX, XXX−XXX

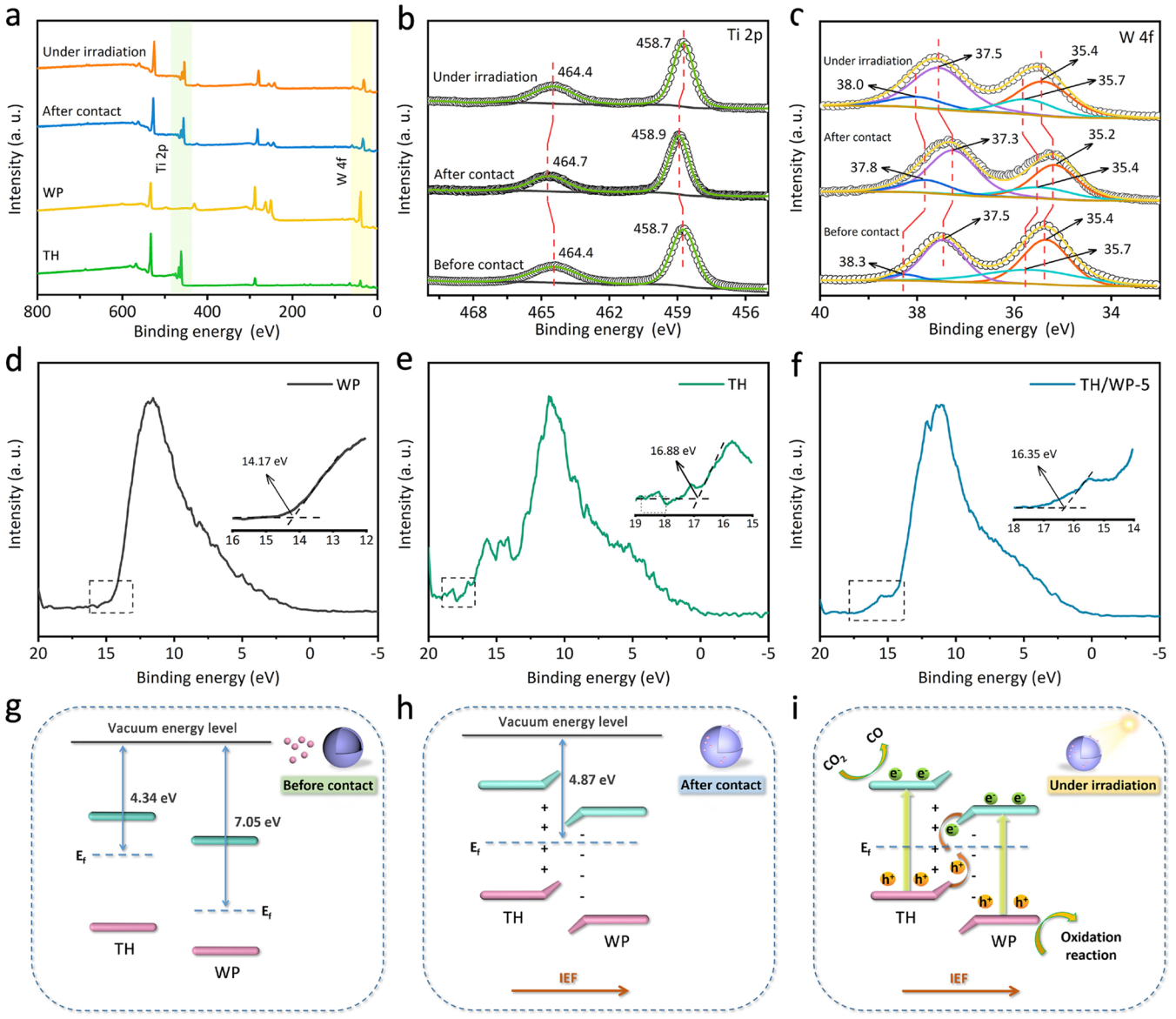

Figure 5. *In situ* XPS spectra of (a) full spectra and high-resolution spectra of (b) Ti and (c) W of the TH/WP-5 composite with and without light irradiation. UPS spectra of the (d) TH, (e) WP, and (f) TH/WP heterojunction. Possible photocatalytic mechanism of the S-scheme TH/WP heterojunction (g) before contact, (h) after contact, and (i) under irradiation.

from CO_2 photoreduction gradually increases over time (Figure 4a). Figure 4b demonstrates that the CO_2 reduction performance shows a volcano-shaped trend with an increase in the level of WP incorporation. The best CO production rate is achieved by TH/WP-5, reaching 4.73 μmol g^{-1} h^{-1}. The CO_2 photoreduction activity of TH/WP-7 can be mainly ascribed to the active catalytic sites and light absorption of the TH shell being hindered by the excess WP. Meanwhile, the TiO_2 nanoparticle-based TP/WP-5 composite exhibits a rather low CO production rate of 1.71 μmol g^{-1} h^{-1} (Figure S7a,b), probably due to the agglomeration of TiO_2 and WO_3 nanoparticles with a flimsy interfacial contact and smaller specific surface area.

The dosage (Figures S8 and S9) and pondus hydrogenii (pH) (Figure S10) effects were further assessed to test the adaptability of the TH/WP-5 sample for CO_2 photoreduction. As a result, a representative 20 mg of TH/WP-5 and neutral conditions (pH ~7) were chosen as the optimal catalyst dosage and reaction condition to make the results more compelling and allow widespread application. To further demonstrate the superiority of the photocatalysts prepared in this work, a comparison of the photocatalytic CO_2 reduction performance with those from other previously reported related works is provided in Table S2.

To further investigate the stability of the prepared photocatalyst, a long-term CO_2 photoreduction experiment was performed with the TH/WP composite. The results (Figure 4c) show that the optimized TH/WP-5 sample can continuously reduce CO_2 to CO within 16 h, and the amount of CO production increases linearly. In addition, the XRD pattern (Figure 4d), XPS spectra (Figure S11), and TEM image (Figure S12) of the TH/WP-5 composite collected after the photocatalytic reaction are well matched with those of the fresh sample, strongly confirming that the prepared TH/WP-5 sample is a promising CO_2 reduction photocatalyst with long-term photostabilization.[38]

https://doi.org/10.1021/acs.inorgchem.2c02443
Inorg. Chem. XXXX, XXX, XXX−XXX

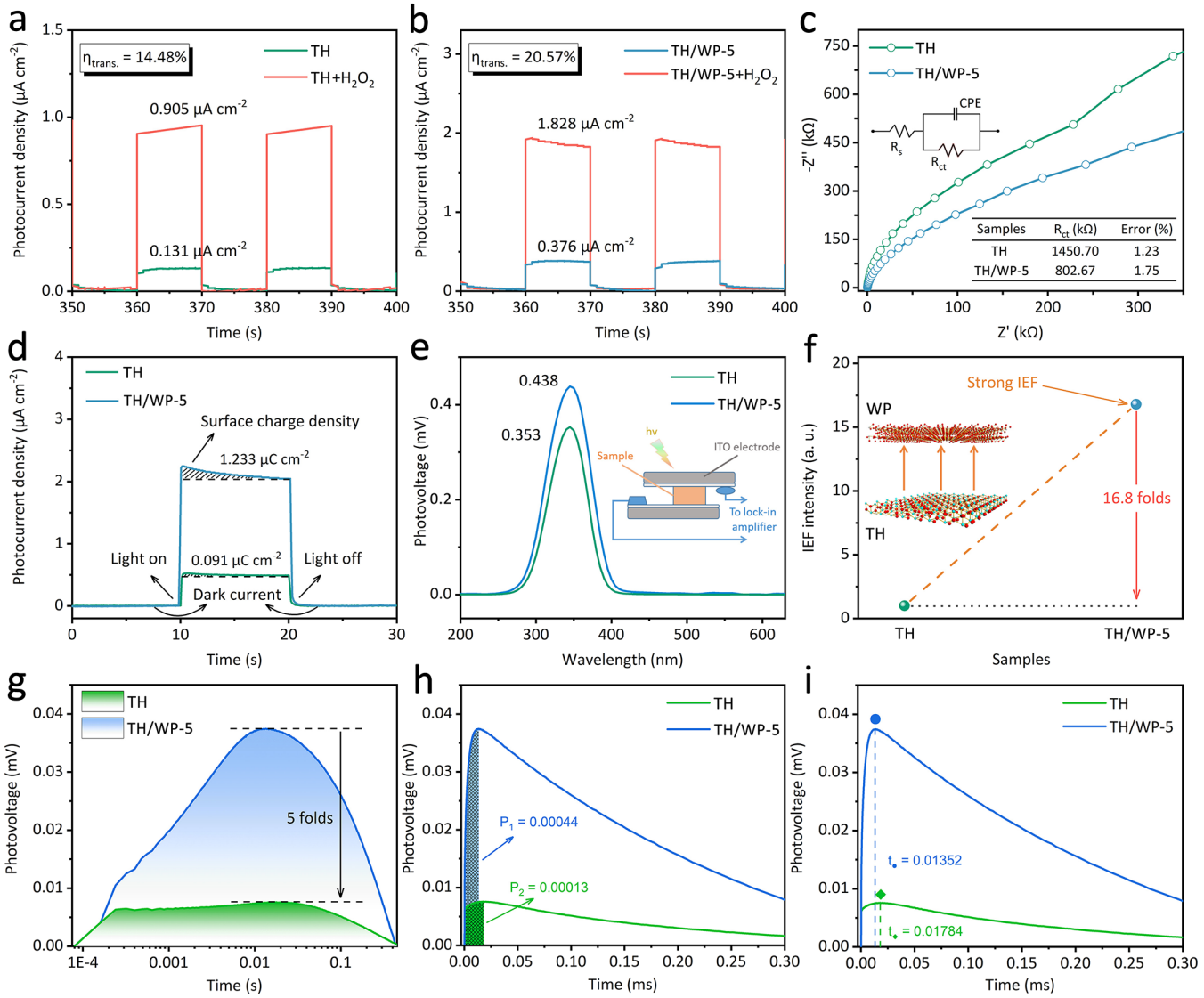

Figure 6. Transient photocurrent density of the (a) TH and (b) TH/WP-5 samples with and without the addition of H_2O_2. (c) EIS Nyquist plots, (d) surface charge densities, (e) SS-SPV spectra, and (f) IEF intensities of the TH and TH/WP-5 samples. (g) TS-SPV spectra, (h) charge extraction efficiencies, and (i) maximum charge extraction times of the TH and TH/WP-5 samples.

To elaborate the S-scheme heterojunction mechanism, *in situ* XPS technology was used to examine the TH/WP-5 composite. As shown in Figure 5a, all of the Ti, O, and W elements could be seen in the full XPS spectra of the TH/WP-5 composite before and after irradiation. In Figure 5b, the binding energies of Ti 2p spectra in the TH/WP-5 composite exhibit a negative shift (~0.3 eV) under light irradiation, while the W element in the TH/WP-5 composite (Figure 5c) shows a positive binding energy shift of ~0.3 eV compared to that in the dark. These interesting results suggest that the TH with a higher Fermi level can act as the electron donor in the TH/WP-5 composite when two components contact each other, leading to the transfer of electrons from TH to WP. When the light turns on, the TH can serve as an electron acceptor and the photogenerated electrons would migrate from WP to TH. Finally, the invalid electrons from the CB of the WP can transfer to the valence band (VB) of the TH to recombine with reserved holes; thereby, the electrons with the greatest reduction capacity can remain on the CB of TH, and the holes with superior oxidation capacity would be left on VB of the WP, fully satisfying the kinetic requirements of CO_2 photoreduction. The charge transfer pathways of the interface of the TH/WP-5 composite can be evidenced by the binding energy shifts in the *in situ* XPS spectra, which strongly support the S-scheme mechanism for the TH/WP-5 composite.[39,40]

The energy band structure of the prepared photocatalysts should be seen as a basis for the carrier transfer pathway. The ultraviolet−visible diffuse reflectance spectrum (DRS) was recorded to determine the energy band structure and light absorption capacities of as-synthesized samples (Figure S13a).[41] Apparently, the WP exhibits a broad and strong light absorption in comparison to that of the pristine TH. The energy gaps of the TH and WP are estimated to be 3.26 and 2.85 eV, respectively, via Tauc plots (Figure S13b). Moreover, a slight enhancement of light absorption could be observed for the TH/WP-*x* heterojunctions. The Mott−Schottky measurements with three different frequencies of prepared samples are further conducted, demonstrating that the flat band positions (E_{fb}) of the TH and WP are −0.90 and −0.08 V versus Ag/AgCl, respectively (Figure S13c), because the bottom of the

https://doi.org/10.1021/acs.inorgchem.2c02443
Inorg. Chem. XXXX, XXX, XXX−XXX

CB is generally 0.3 V more negative than the E_{fb} in n-type semiconductors. Finally, the CB positions can be estimated to be −0.60 and 0.21 V versus NHE for the TH and WP, respectively. As displayed in Figure S13d, such an energy band structure strongly supports the formation of an S-scheme heterojunction between the TH and WP.

To further clarify the S-scheme mechanism of the TH/WP heterojunction, the work functions (W_F) of the obtained samples were measured by ultraviolet photoelectron spectroscopy (UPS). The W_F could help to determine the Fermi level positions (E_{Fermi}) of the TH, WP, and TH/WP-5 samples. The W_F and secondary electron cutoff edge (E_{cutoff}) could be obtained from the UPS spectra. Then, the corresponding W_F value could be calculated by eq 1:[42]

$$W_F = h\nu - E_{cutoff} \quad (1)$$

where $h\nu$ (21.22 eV) represents the photoelectron energy of the He I excitation light source used in the UPS measurement.[43,44] As shown in Figure 5d−f, the binding energies of the E_{cutoff} of the WP, TH, and TH/WP-5 samples are shown to be 14.17, 16.88, and 16.35 eV, respectively. Ultimately, the W_F values of the WP, TH, and TH/WP-5 samples can be estimated to be 7.05, 4.34, and 4.87 eV, respectively, indicating the Fermi level of WP is lower than that of TH.

Combining the energy band structure with work functions analysis, we can deduce the charge transfer pathway of the TH/WP-5 heterojunction as an S-scheme heterojunction mechanism. Before contact, the band structure and Fermi levels of the TH and WP are presented in Figure 5g. Then, the tight contact of two semiconductor components leads to the interfacial electron transfer from TH to WP until the E_f tends to equilibrium,[45] resulting in intermediate E_{Fermi} and W_F values of the TH/WP-5 composite, and an IEF occurred at the interface between the TH and WP (Figure 5h). Under light irradiation, the strong interfacial IEF can impel the invalid photogenerated electrons from the CB of the WP to recombine with holes at the VB of the TH, leading to the effective separation of photogenerated carriers (Figure 5i). These results show that the construction of the TH/WP S-scheme heterojunctions with strong IEF could inhibit the recombination of photogenerated charges and maintain the highest redox capacity to meet the kinetic requirements of CO_2 photoreduction.

Furthermore, the separation and transfer kinetics of photogenerated charges were studied to clarify the main factors for improving photocatalytic CO_2 reduction performance. The photoelectrochemical measurements were conducted to elucidate the separation efficiency of photogenerated charges in the TH/WP heterojunction. As revealed in panels a and b of Figure 6, the transient photocurrent measurements indicate that the TH/WP composite possesses a photocurrent density that is much higher than that of the pristine TH, implying faster separation of photogenerated carriers in the TH/WP heterojunction. Simultaneously, the surface charge transfer efficiency (η_{trans}) is investigated by adding a fast electron scavenger (H_2O_2) to the electrolyte solution.[46] The η_{trans} can be calculated by the ratio of photocurrents (J) detected in H_2O and H_2O_2 electrolytes (the calculation details are presented in the Supporting Information). As expected, the positive photocurrent intensities of the TH and TH/WP-5 samples increase with the addition of H_2O_2. Accordingly, the η_{trans} values of the TH and TH/WP-5 samples are determined to be 14.48% and 20.57%, respectively, demonstrating that the TH/WP-5 composite exhibits a surface charge transfer efficiency that is greater than that of the pristine TH. In addition, the arc radius of the Nyquist curve from electrochemical impedance spectroscopy (EIS) for the TH/WP-5 composite is smaller than that of the pristine TH (Figure 6c). The corresponding charge transfer resistance (R_{ct}) of the TH/WP-5 composite is estimated to be only 802.67 kΩ by fitting EIS plots, much lower than that of the pure TH (1450.70 kΩ), reflecting a smaller photogenerated charge migration resistance and more rapid carrier transfer through the tight interfacial contact in the TH/WP-5 S-scheme heterojunction.[47,48] The time-resolved fluorescence spectroscopy (TR-PL) spectra in Figure S14 show that the average lifetime of the TH/WP-5 composite (0.536 ns) is much shorter than that of the pure TH (1.676 ns), suggesting that the efficiency of separation of photogenerated carriers is improved in the TH/WP-5 composite.[49,50]

Notably, the integral value is proportional to the number of accumulated positive charges on the semiconductor surface determined by subtracting the transient photocurrent density from the steady-state photocurrent versus time (Figure 6d). Meanwhile, the surface photovoltage values of the TH and TH/WP-5 samples are 0.353 and 0.438 mV, respectively, as revealed in the SS-SPV spectra (Figure 6e). Finally, the IEF strength (F_s) can be determined by using eq 2:[51]

$$F_s = (-2V_s\rho/\varepsilon\varepsilon_0)^{1/2} \quad (2)$$

where V_s and ρ represent the surface voltage and surface charge density, respectively, and ε and ε_0 are the low-frequency dielectric constant and the permittivity of free space, respectively. With two constants of ε and ε_0 in eq 2, the IEF strength is generally influenced by the surface voltage and charge density. Thereby, the IEF intensity of the TH/WP-5 composite is estimated to be 16.80 times that of the pure TH (Figure 6f).

Furthermore, the transient-state surface photovoltage (TS-SPV) technology was applied to penetrate the interfacial charge transfer kinetics in the TH/WP-5 heterojunction. In a rapid respond range (from 0.0001 to 0.45 s), the TH/WP-5 photocatalyst exhibits a photovoltage signal 5-fold higher than that of the pure TH (Figure 6g), indicating that a stronger IEF in the TH/WP-5 S-scheme heterojunction is beneficial for promoting the separation and transfer of photogenerated charges.[52,53] In Figure 6h, the shaded integral area (P) indicates the number of extracted electrons. Consequently, the obtained P_1 for the TH/WP-5 composite is 0.00044, which is 3.4 times higher than that of the pure TH (P_2, 0.00013), suggesting that more photogenerated charges can be successfully transferred to the TH/WP-5 surface compared to that in the pure TH. Moreover, the maximum charge extraction time (τ) reflects the charge transfer rate, which plays such a vital role in the photogenerated charge transfer process. Figure 6i shows that the more rapid charge transfer efficiency of the TH/WP-5 composite ($\tau_{\bullet}$ = 0.01352 ms) relative to that of the pure TH ($\tau_{\blacklozenge}$ = 0.01784 ms).[54] These results are consistent with the TR-PL analysis (Figure S14), which could be regarded as strong evidence for the IEF in the TH/WP-5 heterojunction. Because of the strong IEF intensity and low charge transfer resistance, the charge separation efficiency of the TH/WP-5 heterojunction reaches 20.57%, which is ∼1.42 times that of the pure TH. These results lead us to conclude that the greater number photogenerated charges in the TH/WP-5 heterojunction could separate and transfer in a shorter

https://doi.org/10.1021/acs.inorgchem.2c02443
Inorg. Chem. XXXX, XXX, XXX−XXX

time, leading to an efficient photocatalytic CO_2 reduction performance.

On the basis of the experimental results presented above, a possible photocatalytic CO_2 reduction pathway over the TH/WP-5 heterojunction is proposed in Figure 7. To equilibrate

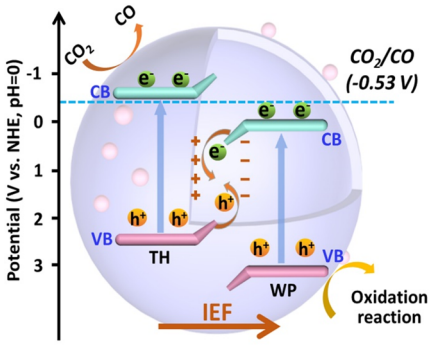

Figure 7. Proposed mechanism for CO_2 photoreduction over the TH/WP-5 composite.

the Fermi energy levels of two semiconductor components, the strong interaction between the TH/WP-5 heterostructures would lead to charge transfer through the contact interface, until a giant IEF formed.[55] First, the rich active sites could be provided by the dual-shell hollow-sphere structure of the TH/WP-5 composite. Then, under light irradiation, the photogenerated electrons from the CB of the WP could recombine with holes in the VB of the TH under the effect of IEF, leaving the charges with the highest redox potential in the CB of the TH and the VB of the WP. Notably, a large number of photogenerated electrons are verified to migrate to the photocatalyst surface due to the strong IEF. Meanwhile, the rich surface-active sites on the dual-shell hollow-sphere structure are beneficial for CO_2 adsorption and activation. With photogenerated electrons, and H^+ from water, the activated CO_2 would go through a continuous process: $CO_2 + 2H^+ + 2e^- \rightarrow CO + H_2O$.[56,57]

3. CONCLUSIONS

In summary, a TiO_2 hollow-sphere-based S-scheme heterojunction was designed and synthesized to study the kinetic mechanism of photogenerated charge transfer and CO_2 photoreduction. For the fabricated S-scheme heterojunction photocatalyst, the IEF intensity and charge separation efficiency of the optimized TH/WP composite were determined to be 16.80 and 1.42 times higher, respectively, than those of the pristine TH. Meaningfully, the TS-SPV results revealed a great advantage of the TH/WP composite in terms of its charge extraction rate (~3.38 times higher than that of the TH) and maximum extraction time (0.01352 ms) compared to those of the pure TH. In brief, the synergetic advantages of the strong charge driving force induced by the giant IEF, S-scheme pathway, and abundant active sites could accelerate charge separation and transfer and maintain high redox ability for realizing an improved kinetic process in CO_2 photoreduction and promote photocatalytic performance. This work explored the interfacial charge transfer insights based on S-scheme heterojunction photocatalysts through a series of photoelectrochemical tests and provided a new vision for further mechanistic investigation of the photocatalytic CO_2 reduction reaction.

ASSOCIATED CONTENT

Supporting Information

The Supporting Information is available free of charge at https://pubs.acs.org/doi/10.1021/acs.inorgchem.2c02443.

Experimental details, lattice fringe (Figures S1 and S2), SEM and XRD results for the TP (Figure S3), BET and BJH results (Figure S4), photocatalytic equipment (Figures S5 and S6), photocatalytic activity of compared samples and conditions (Figures S7−S10), XPS spectra (Figure S11) and TEM images (Figure S12) of the recycled sample, DRS and band structure (Figure S13), TR-PL spectra (Figure S14), contents of actual elements (Table S1), and a comparison of photocatalytic performance (Table S2) (PDF)

AUTHOR INFORMATION

Corresponding Authors

Qinqin Liu − *School of Materials Science and Engineering, Jiangsu University, Zhenjiang, Jiangsu 212013, P. R. China;* orcid.org/0000-0002-7855-0438; Email: qqliu@ujs.edu.cn

Tingting Kong − *College of Chemistry and Materials, Engineering Research Center of Carbon Neutrality, Anhui Normal University, Wuhu, Anhui 241002, P. R. China;* Email: 793255775@qq.com

Weikang Wang − *School of Materials Science and Engineering, Jiangsu University, Zhenjiang, Jiangsu 212013, P. R. China;* Email: wangwk@issp.ac.cn

Authors

Haiwei Su − *School of Materials Science and Engineering, Jiangsu University, Zhenjiang, Jiangsu 212013, P. R. China*

Haopeng Jiang − *School of Materials Science and Engineering, Jiangsu University, Zhenjiang, Jiangsu 212013, P. R. China*

Lijuan Sun − *School of Materials Science and Engineering, Jiangsu University, Zhenjiang, Jiangsu 212013, P. R. China*

Zhongxi Lu − *School of Materials Science and Engineering, Jiangsu University, Zhenjiang, Jiangsu 212013, P. R. China*

Hua Tang − *School of Environmental Science and Engineering, Qingdao University, Qingdao, Shandong 266071, P. R. China;* orcid.org/0000-0002-3132-4185

Lele Wang − *School of Materials Science and Engineering, Jiangsu University, Zhenjiang, Jiangsu 212013, P. R. China*

Complete contact information is available at: https://pubs.acs.org/10.1021/acs.inorgchem.2c02443

Notes

The authors declare no competing financial interest.

ACKNOWLEDGMENTS

This work was financially supported by the National Natural Science Foundation of China (21972058, 51902253, and 22102064) and the Natural Science Foundation of Shaanxi Province (2020JQ-778). H.T. appreciates the support from the Taishan Youth Scholar Program of Shandong Province. L.W. was supported by the Open Project Program of the State Key Laboratory of Photocatalysis on Energy and Environment (SKLPEE-KF202102), Fuzhou University.

https://doi.org/10.1021/acs.inorgchem.2c02443
Inorg. Chem. XXXX, XXX, XXX−XXX

REFERENCES

(1) Fu, J.; Jiang, K.; Qiu, X.; Yu, J.; Liu, M. Product selectivity of photocatalytic CO_2 reduction reactions. *Mater. Today* **2020**, *32*, 222−243.

(2) Jiang, Y.; Liao, J.-F.; Chen, H.-Y.; Zhang, H.-H.; Li, J.-Y.; Wang, X.-D.; Kuang, D.-B. All-Solid-State Z-Scheme α-Fe_2O_3/Amine-RGO/$CsPbBr_3$ Hybrids for Visible-Light-Driven Photocatalytic CO_2 Reduction. *Chem.* **2020**, *6* (3), 766−780.

(3) Wang, S.; Han, X.; Zhang, Y.; Tian, N.; Ma, T.; Huang, H. Inside-and-Out Semiconductor Engineering for CO_2 Photoreduction: From Recent Advances to New Trends. *Small Struct.* **2021**, *2*, 2000061.

(4) Zhao, J.; Guo, X.; Shi, R.; Waterhouse, G. I. N.; Zhang, X.; Dai, Q.; Zhang, T. NiFe Nanoalloys Derived from Layered Double Hydroxides for Photothermal Synergistic Reforming of CH_4 with CO_2. *Adv. Funct. Mater.* **2022**, *32*, 2204056.

(5) Wang, M.; Shen, M.; Jin, X.; Tian, J.; Shao, Y.; Zhang, L.; Li, Y.; Shi, J. Exploring the enhancement effects of hetero-metal doping in CeO_2 on CO_2 photocatalytic reduction performance. *Chem. Eng. J.* **2022**, *427*, 130987.

(6) Di, J.; Lin, B.; Tang, B.; Guo, S.; Zhou, J.; Liu, Z. Engineering Cocatalysts onto Low-Dimensional Photocatalysts for CO_2 Reduction. *Small Struct.* **2021**, *2*, 2100046.

(7) Li, P.; He, T. Recent advances in zinc chalcogenide-based nanocatalysts for photocatalytic reduction of CO_2. *J. Mater. Chem. A* **2021**, *9*, 23364−23381.

(8) Liu, S.; Jiang, T.; Fan, M.; Tan, G.; Cui, S.; Shen, X. Nanostructure rod-like TiO_2-reduced graphene oxide composite aerogels for highly-efficient visible-light photocatalytic CO_2 reduction. *J. Alloys Compd.* **2021**, *861*, 158598.

(9) Li, N.; Chen, X.; Wang, J.; Liang, X.; Ma, L.; Jing, X.; Chen, D.-L.; Li, Z. ZnSe Nanorods−$CsSnCl_3$ Perovskite Heterojunction Composite for Photocatalytic CO_2 Reduction. *ACS Nano* **2022**, *16*, 3332−3340.

(10) Zhang, L.; Zhang, J.; Yu, H.; Yu, J. Emerging S-Scheme Photocatalyst. *Adv. Mater.* **2022**, *34* (11), 2107668.

(11) Cheng, L.; Yue, X.; Fan, J.; Xiang, Q. Site-Specific Electron-Driving Observations of CO_2-to-CH_4 Photoreduction on Co-Doped CeO_2/Crystalline Carbon Nitride S-Scheme Heterojunctions. *Adv. Mater.* **2022**, *34*, 2200929.

(12) Moon, H. S.; Hsiao, K. C.; Wu, M. C.; Yun, Y.; Hsu, Y. J.; Yong, K. Spatial Separation of Cocatalysts on Z-Scheme Organic/Inorganic Heterostructure Hollow-spheres for Enhanced Photocatalytic H_2 Evolution and In-Depth Analysis of the Charge-Transfer Mechanism. *Adv. Mater.* **2022**, 2200172.

(13) Chen, Q.; Lan, X.; Chen, K.; Ren, Q.; Shi, J. Construction of WO_3/$CsPbBr_3$ S-scheme heterojunction via electrostatic Self-assembly for efficient and Long-Period photocatalytic CO_2 reduction. *J. Colloid Interface Sci.* **2022**, *616*, 253−260.

(14) Xia, P.; Cao, S.; Zhu, B.; Liu, M.; Shi, M.; Yu, J.; Zhang, Y. Designing a 0D/2D S-Scheme Heterojunction over Polymeric Carbon Nitride for Visible-Light Photocatalytic Inactivation of Bacteria. *Angew. Chem., Int. Ed.* **2020**, *59* (13), 5218−5225.

(15) Jiang, Y.; Wang, Y.; Zhang, Z.; Dong, Z.; Xu, J. 2D/2D $CsPbBr_3$/BiOCl Heterojunction with an S-Scheme Charge Transfer for Boosting the Photocatalytic Conversion of CO_2. *Inorg. Chem.* **2022**, *61* (27), 10557−10566.

(16) FUJISHIMA, A.; HONDA, K. Electrochemical Photolysis of Water at a Semiconductor Electrode. *Nature* **1972**, *238*, 37−38.

(17) Ke, Y.; Liang, Q.; Zhao, S.; Zhang, Z.; Li, X.; Li, Z. In Situ Self-Assembled ZIF-67/MIL-125-Derived Co_3O_4/TiO_2 p-n Heterojunctions for Enhanced Photocatalytic CO_2 Reduction. *Inorg. Chem.* **2022**, *61* (5), 2652−2661.

(18) Son, H. J.; Pac, C.; Kang, S. O. Inorganometallic Photocatalyst for CO_2 Reduction. *Acc. Chem. Res.* **2021**, *54* (24), 4530−4544.

(19) Abdullah, H.; Khan, M. M. R.; Ong, H. R.; Yaakob, Z. Modified TiO_2 photocatalyst for CO_2 photocatalytic reduction: An overview. *J. CO2 Util.* **2017**, *22*, 15−32.

(20) Jin, L.; Shaaban, E.; Bamonte, S.; Cintron, D.; Shuster, S.; Zhang, L.; Li, G.; He, J. Surface Basicity of Metal@TiO_2 to Enhance Photocatalytic Efficiency for CO_2 Reduction. *ACS Appl. Mater. Interfaces* **2021**, *13* (32), 38595−38603.

(21) Gong, H.; Wang, L.; Zhou, K.; Zhang, D.; Zhang, Y.; Adamaki, V.; Sergejevs, A.; Bowen, C. Improved photocatalytic performance of gradient reduced TiO_2 ceramics with aligned pore channels. *Adv. Powder Mater.* **2022**, *1* (3), 100025.

(22) Liu, M.; Zheng, L.; Bao, X.; Wang, Z.; Wang, P.; Liu, Y.; Cheng, H.; Dai, Y.; Huang, B.; Zheng, Z. Substrate-dependent ALD of Cu_x on TiO_2 and its performance in photocatalytic CO_2 reduction. *Chem. Eng. J.* **2021**, *405*, 126654.

(23) Di, T.; Zhang, J.; Cheng, B.; Yu, J.; Xu, J. Hierarchically nanostructured porous TiO_2(B) with superior photocatalytic CO_2 reduction activity. *Sci. China Chem.* **2018**, *61*, 344−350.

(24) Ma, Y.; Yi, X.; Wang, S.; Li, T.; Tan, B.; Chen, C.; Majima, T.; Waclawik, E. R.; Zhu, H.; Wang, J. Selective photocatalytic CO_2 reduction in aerobic environment by microporous Pd-porphyrin-based polymers coated hollow TiO_2. *Nat. Commun.* **2022**, *13*, 1400.

(25) She, P.; Guan, B.; Sheng, J.; Qi, Y.; Qiao, G.; Rui, H.; Lu, G.; Qin, J.-S.; Rao, H. Bioinspired spike-like double yolk-shell structured TiO_2@$ZnIn_2S_4$ for efficient photocatalytic CO_2 reduction. *Catal. Sci. Technol.* **2022**, *12*, 1092−1099.

(26) Sun, B.; Bu, J.; Du, Y.; Chen, X.; Li, Z.; Zhou, W. O, S-Dual-Vacancy Defects Mediated Efficient Charge Separation in $ZnIn_2S_4$/Black TiO_2 Heterojunction Hollow-spheres for Boosting Photocatalytic Hydrogen Production. *ACS Appl. Mater. Interfaces* **2021**, *13*, 37545−37552.

(27) Wang, L.; Zhu, B.; Cheng, B.; Zhang, J.; Zhang, L.; Yu, J. *In-situ* preparation of TiO_2/N-doped graphene hollow-sphere photocatalyst with enhanced photocatalytic CO_2 reduction performance. *Chin. J. Catal.* **2021**, *42*, 1648−1658.

(28) Zhang, Z.; Cao, Y.; Zhang, F.; Li, W.; Li, Y.; Yu, H.; Wang, M.; Yu, H. Tungsten oxide quantum dots deposited onto ultrathin $CdIn_2S_4$ nanosheets for efficient S-scheme photocatalytic CO_2 reduction via cascade charge transfer. *Chem. Eng. J.* **2022**, *428*, 131218.

(29) Wang, L.; Cheng, B.; Zhang, L.; Yu, J. *In situ* Irradiated XPS Investigation on S-Scheme TiO_2@$ZnIn_2S_4$ Photocatalyst for Efficient Photocatalytic CO_2 Reduction. *Small* **2021**, *17* (41), 2103447.

(30) Chen, X.; Wang, J.; Chai, Y.; Zhang, Z.; Zhu, Y. Efficient Photocatalytic Overall Water Splitting Induced by the Giant Internal Electric Field of a g-C_3N_4/rGO/PDIP Z-Scheme Heterojunction. *Adv. Mater.* **2021**, *33* (7), 2007479.

(31) Wang, X.; Chen, F.; Yang, M.; Guo, L.; Xie, N.; Kou, X.; Song, Y.; Wang, Q.; Sun, Y.; Lu, G. Dispersed WO_3 nanoparticles with porous nanostructure for ultrafast toluene sensing. *Sens. Actuators B Chem.* **2019**, *289*, 195−206.

(32) Xiao, J.; Chen, C.; Chen, S.; Liu, H.; Peng, T. Insight into the significantly enhanced photocatalytic CO_2 reduction performance of Pt/MnO dual cocatalysts on sea-urchin-like anatase TiO_2 microspheres. *Chem. Eng. J.* **2021**, *425*, 131627.

(33) Gong, H.; Li, Y.; Li, H.; Jin, Z. 2D CeO_2 and a Partially Phosphated 2D Ni-Based Metal−Organic Framework Formed an S-Scheme Heterojunction for Efficient Photocatalytic Hydrogen Evolution. *Langmuir* **2022**, *38* (6), 2117−2131.

(34) Han, X.; Lu, B.; Huang, X.; Liu, C.; Chen, S.; Chen, J.; Zeng, Z.; Deng, S.; Wang, J. Novel p- and n-type S-scheme Heterojunction Photocatalyst for Boosted CO_2 Photoreduction Activity. *Appl. Catal. B Environ.* **2022**, *316*, 121587.

(35) Wang, L.; Tang, G.; Liu, S.; Dong, H.; Liu, Q.; Sun, J.; Tang, H. Interfacial active-site-rich 0D Co_3O_4/1D TiO_2 p-n heterojunction for enhanced photocatalytic hydrogen evolution. *Chem. Eng. J.* **2022**, *428*, 131338.

(36) Ding, Y.; Wei, D.; He, R.; Yuan, R.; Xie, T.; Li, Z. Rational design of Z-scheme PtS-$ZnIn_2S_4$/WO_3-MnO_2 for overall photocatalytic water splitting under visible light. *Appl. Catal. B Environ.* **2019**, *258*, 117948.

https://doi.org/10.1021/acs.inorgchem.2c02443
Inorg. Chem. XXXX, XXX, XXX−XXX

(37) He, F.; Meng, A.; Cheng, B.; Ho, W.; Yu, J. Enhanced photocatalytic H_2-production activity of WO_3/TiO_2 step-scheme heterojunction by graphene modification. *Chin. J. Catal.* **2020**, *41* (1), 9−20.
(38) Su, H.; Yu, X.; Wang, W.; Wang, L.; Tang, H.; Liu, Q. A 2D bimetallic Ni-Co hydroxide monolayer cocatalyst for boosting photocatalytic H_2 evolution. *Chem. Commun.* **2022**, *58* (42), 6180−6183.
(39) Yang, J.; Sun, J.; Chen, S.; Lan, D.; Li, Z.; Li, Z.; Wei, J.; Yu, Z.; Zhu, H.; Wang, S.; Hou, Y. S-scheme 1T phase $MoSe_2$/AgBr heterojunction toward antibiotic degradation: Photocatalytic mechanism, degradation pathways, and intermediates toxicity evaluation. *Sep. Purif. Technol.* **2022**, *290*, 120881.
(40) Li, X.; Kang, B.; Dong, F.; Zhang, Z.; Luo, X.; Han, L.; Huang, J.; Feng, Z.; Chen, Z.; Xu, J.; Peng, B.; Wang, Z. L. Enhanced photocatalytic degradation and H_2/H_2O_2 production performance of S-pCN/$WO_{2.72}$ S-scheme heterojunction with appropriate surface oxygen vacancies. *Nano Energy* **2021**, *81*, 105671.
(41) Han, G.; Xu, F.; Cheng, B.; Li, Y.; Yu, J.; Zhang, L. Enhanced Photocatalytic H_2O_2 Production over Inverse Opal ZnO@Polydopamine S-Scheme Heterojunctions. *Acta Phys.-Chim. Sin.* **2022**, *38* (7), 2112037.
(42) Wang, C.; Wang, L.; Jin, J.; Liu, J.; Li, Y.; Wu, M.; Chen, L.; Wang, B.; Yang, X.; Su, B.-L. Probing effective photocorrosion inhibition and highly improved photocatalytic hydrogen production on monodisperse PANI@CdS core-shell nanospheres. *Appl. Catal. B Environ.* **2016**, *188*, 351−359.
(43) Bai, J.; Shen, R.; Chen, W.; Xie, J.; Zhang, P.; Jiang, Z.; Li, X. Enhanced photocatalytic H_2 evolution based on a $Ti_3C_2/Zn_{0.7}Cd_{0.3}S/Fe_2O_3$ Ohmic/S-scheme hybrid heterojunction with cascade 2D coupling interfaces. *Chem. Eng. J.* **2022**, *429*, 132587.
(44) Huang, S.; Ouyang, T.; Zheng, B.-F.; Dan, M.; Liu, Z.-Q. Enhanced Photoelectrocatalytic Activities for CH_3OH-to-HCHO Conversion on Fe_2O_3/MoO_3: Fe-O-Mo Covalency Dominates the Intrinsic Activity. *Angew. Chem., Int. Ed.* **2021**, *60*, 9546−9552.
(45) Wang, Z.; Liu, R.; Zhang, J.; Dai, K. S-scheme Porous g-C_3N_4/Ag_2MoO_4 Heterojunction Composite for CO_2 Photoreduction. *Chin. J. Struct. Chem.* **2022**, *41*, 2206015−2206022.
(46) Liu, G.; Shi, J.; Zhang, F.; Chen, Z.; Han, J.; Ding, C.; Chen, S.; Wang, Z.; Han, H.; Li, C. A tantalum nitride photoanode modified with a hole-storage layer for highly stable solar water splitting. *Angew. Chem., Int. Ed.* **2014**, *53* (28), 7295−7299.
(47) Hu, Y.; Yu, X.; Liu, Q.; Wang, L.; Tang, H. Highly metallic Co-doped MoS_2 nanosheets as an efficient cocatalyst to boost photoredox dual reaction for H_2 production and benzyl alcohol oxidation. *Carbon* **2022**, *188*, 70−80.
(48) Yang, M.; Wang, P.; Li, Y.; Tang, S.; Lin, X.; Zhang, H.; Zhu, Z.; Chen, F. Graphene aerogel-based NiAl-LDH/g-C_3N_4 with ultratight sheet-sheet heterojunction for excellent visible-light photocatalytic activity of CO_2 reduction. *Appl. Catal. B Environ.* **2022**, *306*, 121065.
(49) Che, H.; Gao, X.; Chen, J.; Hou, J.; Ao, Y.; Wang, P. Iodide-Induced Fragmentation of Polymerized Hydrophilic Carbon Nitride for High-Performance Quasi-Homogeneous Photocatalytic H_2O_2 Production. *Angew. Chem., Int. Ed.* **2021**, *60* (48), 25546−25550.
(50) Gao, R.; He, H.; Bai, J.; Hao, L.; Shen, R.; Zhang, P.; Li, Y.; Li, X. Pyrene-benzothiadiazole-based Polymer/CdS 2D/2D Organic/Inorganic Hybrid S-scheme Heterojunction for Efficient Photocatalytic H_2 Evolution. *Chin. J. Struct. Chem.* **2022**, *41*, 2206031−2206038.
(51) Kanata, T.; Matsunaga, M.; Takakura, H.; Hamakawa, Y.; Nishino, T. Photoreflectance Characterization of Built-in Potential in MBE Produced as-grown GaAs Surface. *Proc. SPIE* **1990**, *1286*, 56−65.
(52) Li, Y.; Wu, Q.; Bu, Q.; Zhang, K.; Lin, Y.; Wang, D.; Zou, X.; Xie, T. An effective CdS/Ti-Fe_2O_3 heterojunction photoanode: Analyzing Z-scheme charge-transfer mechanism for enhanced photoelectrochemical water-oxidation activity. *Chin. J. Catal.* **2021**, *42* (5), 762−771.
(53) Ruan, X.; Cui, X.; Cui, Y.; Fan, X.; Li, Z.; Xie, T.; Ba, K.; Jia, G.; Zhang, H.; Zhang, L.; Zhang, W.; Zhao, X.; Leng, J.; Jin, S.; Singh, D. J.; Zheng, W. Favorable Energy Band Alignment of TiO_2 Anatase/Rutile Heterophase Homojunctions Yields Photocatalytic Hydrogen Evolution with Quantum Efficiency Exceeding 45.6%. *Adv. Energy Mater.* **2022**, *12* (16), 2200298.
(54) Li, F.; Liu, Y.; Chen, Q.; Gu, X.; Dong, W.; Zhang, D.; Huang, H.; Mao, B.; Kang, Z.; Shi, W. Transient photovoltage study of the kinetics and synergy of electron/hole co-extraction in MoS_2/Ag-In-Zn-S/carbon dot photocatalysts for promoted hydrogen production. *Chem. Eng. J.* **2022**, *439*, 135759.
(55) Wageh, S.; Al-Ghamdi, A. A.; Liu, L. S-Scheme Heterojunction Photocatalyst for CO_2 Photoreduction. *Acta Phys.-Chim. Sin.* **2021**, *37* (6), 2010024.
(56) Ouyang, T.; Huang, S.; Wang, X.-T.; Liu, Z.-Q. Nanostructures for Electrocatalytic CO_2 Reduction. *Chem. - Eur. J.* **2020**, *26* (62), 14024−14035.
(57) Huang, X.; Gu, W.; Hu, S.; Hu, Y.; Zhou, L.; Lei, J.; Wang, L.; Liu, Y.; Zhang, J. Phosphorus-doped inverse opal g-C_3N_4 for efficient and selective CO generation from photocatalytic reduction of CO_2. *Catal. Sci. Technol.* **2020**, *10*, 3694−3700.

https://doi.org/10.1021/acs.inorgchem.2c02443
Inorg. Chem. XXXX, XXX, XXX−XXX